Original Research

Measurements of Wall Shear Stress and Aortic Pulse Wave Velocity in Swine With Familial Hypercholesterolemia

Andrew L. Wentland, PhD,[1,2]* Oliver Wieben, PhD,[1,2]
Dhanansayan Shanmuganayagam, PhD,[3] Christian G. Krueger, BS,[3]
Jennifer J. Meudt, MS,[3] Daniel Consigny, BS,[2] Leonardo Rivera, BS,[1]
Patrick E. McBride, MD, MPH,[4] Jess D. Reed, PhD,[3] and Thomas M. Grist, MD[1,2]

Purpose: To assess measurements of pulse wave velocity (PWV) and wall shear stress (WSS) in a swine model of atherosclerosis.

Materials and Methods: Nine familial hypercholesterolemic (FH) swine with angioplasty balloon catheter-induced atherosclerotic lesions to the abdominal aorta (injured group) and 10 uninjured FH swine were evaluated with a 4D phase contrast (PC) magnetic resonance imaging (MRI) acquisition, as well as with radial and Cartesian 2D PC acquisitions, on a 3T MR scanner. PWV values were computed from the 2D and 4D PC techniques, compared between the injured and uninjured swine, and validated against reference standard pressure probe-based PWV measurements. WSS values were also computed from the 4D PC MRI technique and compared between injured and uninjured groups.

Results: PWV values were significantly greater in the injured than in the uninjured groups with the 4D PC MRI technique ($P = 0.03$) and pressure probes ($P = 0.02$). No significant differences were found in PWV between groups using the 2D PC techniques ($P = 0.75–0.83$). No significant differences were found for WSS values between the injured and uninjured groups.

Conclusion: The 4D PC MRI technique provides a promising means of evaluating PWV and WSS in a swine model of atherosclerosis, providing a potential platform for developing the technique for the early detection of atherosclerosis.

Key Words: 4D PC MRI; atherosclerosis; pulse wave velocity; wall shear stress; PWV; familial hypercholesterolemia

J. Magn. Reson. Imaging 2015;41:1475–1485.
© 2014 Wiley Periodicals, Inc.

[1]Department of Medical Physics, University of Wisconsin School of Medicine and Public Health, Madison, Wisconsin, USA.

[2]Department of Radiology, University of Wisconsin School of Medicine and Public Health, Madison, Wisconsin, USA.

[3]Department of Animal Science, University of Wisconsin - Madison, Madison, Wisconsin, USA.

[4]Department of Medicine, University of Wisconsin School of Medicine and Public Health, Madison, Wisconsin, USA.

*Address reprint requests to: A.L.W., University of Wisconsin School of Medicine & Public Health, Department of Medical Physics, 1111 Highland Ave., Madison, WI, 53705-2275.
E-mail: alwentland@wisc.edu

CURRENTLY, the standard method of assessing a patient's risk of a cardiovascular event is with the computation of a Framingham Risk Score (FRS) (1). While studies have shown that intima-media thickness measurements with ultrasound provide an insignificant improvement to the FRS (2), the evaluation of the coronary calcium score via computed tomography (CT) has demonstrated a significant improvement to risk assessment beyond that provided by the FRS alone (3). However, several problems exist in the evaluation of atherosclerosis with CT, including the use of ionizing radiation, the absence of calcium in less well-developed plaques and in some advanced plaques, and the lack of any association between the presence of calcium and the stability of a plaque (4,5). Studies have demonstrated that an imaging-based diagnosis of atherosclerosis improves patient compliance and reinforces risk-reducing behaviors (6,7). Therefore, it would be prudent to develop and investigate imaging-based biomarkers that assist in cardiovascular risk assessment without the use of ionizing radiation or dependence on the presence of calcium in the plaques.

In recent years a number of magnetic resonance imaging (MRI)-based biomarkers of atherosclerosis have been explored, including wall shear stress (WSS) and pulse wave velocity (PWV). Studies have shown that areas of low WSS predict the occurrence of

atherosclerotic plaques (8–11). WSS is a measure of drag forces on vessel walls; it is hypothesized that abnormal blood flow patterns, and in turn insufficient wall shear stress, lead to dysfunction of the endothelium (12). Endothelial dysfunction leads to vascular remodeling, such as adaptive intimal thickening, and may progress to advanced atherosclerotic lesions, especially in the presence of hyperlipidemia and hypertension (10). PWV is another MRI-based biomarker of atherosclerosis (13). As arteries are stiffened by the growth of atherosclerotic plaques, the pulse wave of blood down the aorta is accelerated because of the loss of elastic recoil in the vessel, leading to an elevated PWV value (14).

Previous studies on WSS used techniques that were limited in spatiotemporal resolution (15,16), provided limited anatomic coverage (17,18), and/or relied on semiquantitative descriptions of 3D flow patterns (19–23). Since long scan times are required for large coverage and high spatiotemporal resolution, a previous study on PWV (24) sacrificed one or more of these parameters to achieve what they considered a clinically acceptable scan time of 15–20 minutes. Because WSS is derived from the small velocity gradient at the vessel wall, high spatial resolution is needed for accurate measurements. Since PWV is derived from the rapidly propagating wave of blood down the aorta, high temporal resolution is needed to capture accurately the temporal dynamics of this movement. Therefore, an MRI acquisition that provides high spatial and temporal resolution as well as good anatomic coverage could be very beneficial in the evaluation of these biomarkers of atherosclerosis.

Familial hypercholesterolemias (FH) are a group of genetic defects that lead to significantly elevated levels of low-density lipoprotein (LDL) cholesterol. Due to the elevated LDL levels, FH leads to an increased risk of developing atherosclerosis and adverse cardiovascular events (25). The Rapacz FH swine model carries the equivalent alleles for human FH (26–28) and is considered a highly relevant animal model of spontaneous cardiovascular disease (29,30). Furthermore, the genetic proximity of swine to humans (31,32) and the overwhelming anatomical, physiological, and pathophysiological similarities make the model ideal for developing novel imaging applications that can be directly translated to humans. Therefore, FH swine serve as excellent and predictable models for assessing biomarkers of atherosclerosis.

The purpose of this study was to evaluate the measurements of WSS and PWV in the validated Rapacz FH swine model (26–28) using a radially undersampled 4D phase contrast (PC) MRI technique that provides high spatiotemporal resolution, large anatomic coverage, and a scan time on the order of 10 minutes.

MATERIALS AND METHODS

Animal Model

While the Rapacz FH swine model develops atherosclerotic lesions naturally as a function of age and in a manner remarkably similar to the human disease in time course, location, and phenotypic complexity, lesions can also be induced in predictable locations in the model in an accelerated manner using angioplasty balloon injury. As the induced lesion development occurs within the pathophysiological environment of the Rapacz FH swine, the process in the Rapacz FH swine, in contrast to conventional swine (33), more accurately reflects what is observed in human patients (34,35). Given these advantages, the Rapacz FH swine model has been used extensively in cardiovascular research (33–38).

Animal Population and Injury

Ten swine (five males; five females; mean age ± 1 SD = 8.5 ± 0.5 months; mean mass ± 1 SD = 44.0 ± 3.9 kg; mean resting heart rate ± 1 SD = 97 ± 25 bpm) with and 10 swine (five males; five females; mean age ± 1 SD = 11.3 ± 5.7 months; mean mass ± 1 SD = 48.7 ± 19.0 kg; mean resting heart rate ± 1 SD = 101 ± 17 bpm) without an angioplasty balloon catheter-induced vascular injury (uninjured) were recruited into the study. All swine were homozygous for FH and were randomly assigned to either the injured or uninjured groups. The study protocol was approved by the local Institutional Animal Care and Use Committee. One animal (the penultimate injured pig) died secondary to atrial fibrillation during the insertion of a catheter for placing fiber optic pressure probes. Three of the four subsequent/remaining animals (one injured and three uninjured swine) were pretreated with 150 mg of amiodarone intravenously to prevent potential complications due to atrial fibrillation.

FH swine assigned to the injured group were placed on a formulated atherogenic diet (8.9% lard, 0.89% cholesterol, 0.67% sodium cholate) for ~4 weeks prior to the injury; this atherogenic diet further enhanced the level of hypercholesterolemia in these swine and thus helped to accelerate the development of atherosclerotic lesions postinjury. The animals were fasted for 24 hours prior to the injury procedure. Swine with unknown risk for porcine stress syndrome were prophylactically treated with dantrolene sodium (3.6–7.8 mg/kg) orally to prevent potential hyperthermia (39). On the day of injury animals were sedated with telazol (4–9.7 mg/kg) and xylazine (1.7–2.2 mg/kg) intramuscularly. Atropine (0.05 mg/kg) was administered intramuscularly to decrease bronchiole secretions and to abolish vagal reflex during endotracheal intubation. Subsequently, the swine were intubated, shaven, scrubbed, and draped for surgery and ventilated with 1.5% isoflurane (400 cc/breath; 7 breaths/min) to maintain anesthesia. Balloon catheter-induced injury in the vasculature was performed in the supra- and infrarenal aorta (Fig. 1a) via initial placement of a sheath in one of the carotid arteries. Placement of the balloon catheters was performed via fluoroscopic guidance; injury was performed via over-inflation of the balloon and via retracting and advancing the balloon >5 times. Angiography balloons used
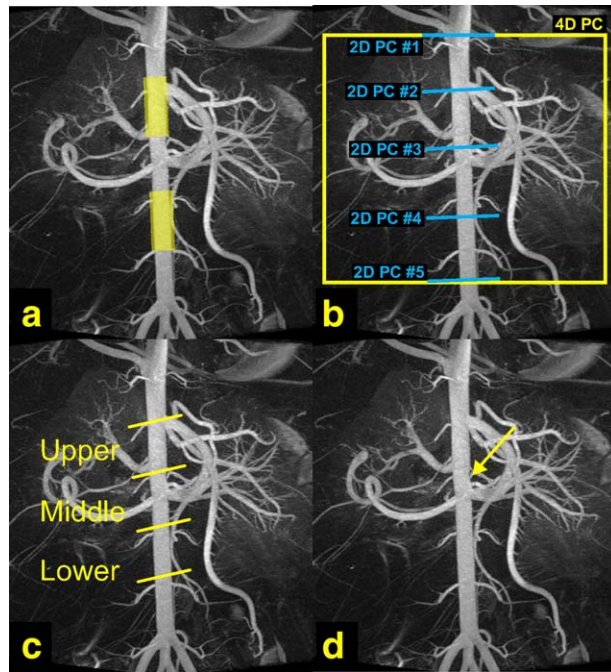
Figure 1. Angiograms provided by C-arm CT. Balloon catheters were deployed within one group of pigs and used to denude the endothelium in two locations, as identified by the yellow boxes in the suprarenal and infrarenal abdominal aorta (**a**). Part **b** demonstrates the prescription of the five 2D planes that were used for the acquisition of radial and Cartesian 2D phase contrast (PC) datasets. Part **b** also depicts the field of view prescribed for the acquisition of the 4D PC dataset. For wall shear stress analysis, values were averaged over three sections (**c**)—the upper (suprarenal aorta), middle (pararenal aorta), and lower (infrarenal aorta) sections. In some angiograms, irregularities could be identified in the areas of injury in the abdominal aorta (**d** - arrow).

in the aorta were either 10 mm × 4 cm or 12 mm × 4 cm, depending on the size of the animal.

Subsequent to the injury the swine were maintained on the atherogenic diet for ~4 weeks. Following this time period the animals were returned for MRI. At this timepoint prophylaxis with dantrolene sodium and sedation with xylazine and telazol were performed as described above. Swine were intubated, shaven, scrubbed, and draped for surgery. General anesthesia was achieved with propofol (8.6–10.7 mg/kg/hr) rather than isoflurane, given that volatile anesthetics, such as isoflurane, have a suppressive effect on hemodynamics (40,41). The swine were then intubated and ventilated (450–600 cc/breath; 9–12 breaths/min). For the uninjured swine, this same sedation and anesthesia procedure was performed. Uninjured swine were maintained on a standard diet prior to the day of imaging. All swine—injured and uninjured—were held off feed for 24 hours prior to the day of imaging. In preparation for imaging, a sheath was placed in one of the carotid arteries and used to introduce pressure probes into the abdominal vasculature. After anesthetization and prior to the MR study, pressure probe-based pulse wave velocity measurements were performed on each swine, as described below. 3D digital subtraction angiography was performed

with C-arm CT in 7/19 swine (five injured; two uninjured) to provide high-resolution angiographic images; these images were used to evaluate the vessels for stenoses and vascular irregularities secondary to hypercholesterolemia and/or balloon-catheter-induced injury. 3D digital subtraction angiography was not performed in other swine due to monetary constraints.

C-Arm CT

3D digital subtraction angiographic (DSA) images (Fig. 1) were obtained on 7/19 animals with a C-arm CT system (Artis zeego; Siemens, Erlangen, Germany). Image acquisition required two 5-second rotations—one rotation for a mask and the other rotation with the injection of iopamidol (370 mgI/mL; Isovue 370; Bracco Diagnostics, Princeton, NJ) into the jugular vein following an appropriate delay time. Reconstruction of the data was performed as previously described (42,43). The acquisition was performed in the abdominal aorta (Fig. 1). Images were evaluated for the presence of stenoses in the vasculature.
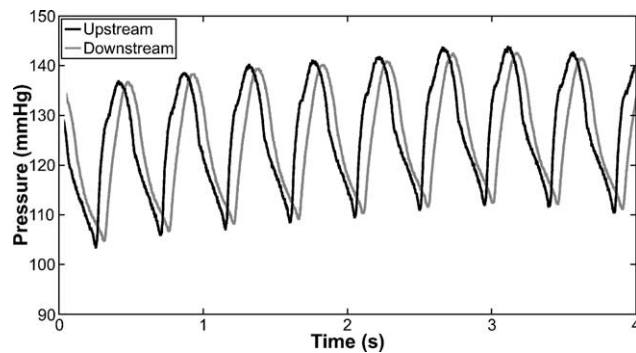
Pressure Probes

Two fiber optic pressure probes (opSens, Quebec, Canada) with the Fabry-Perot interferometer configuration (44) were bound together with Tegaderm (3M, St. Paul, MN); the tips of the two probes were separated by a distance of 10 cm. These probes sense pressure via a microelectromechanical system (MEMS), which houses a diaphragm that deflects in proportion to the amount of strain imparted on it.

The probes were advanced through the sheath placed in the carotid artery and centered over the renal arteries such that the upstream probe was 5 cm superior to the takeoff of the renal arteries; placement was performed with fluoroscopic guidance and the simultaneous advancement of a radiopaque catheter that was retracted following placement. Pressure waveforms over the cardiac cycle were obtained from both probes simultaneously with a sampling rate of 1 kHz (Fig. 2).

The temporal distance between the two flow waveforms can be determined by fitting a line to data points between 10 and 40% of the maximum value of any one cycle of the waveforms. Note that this range of values (10–40%) is different than that used for PWV measurements via flow waveforms (20–80%); 10–40% was used because the shape of the pressure waveform is different than a flow waveform and using 20–80% would lead to an improper fit of the waveforms' upstroke. With a line fitted to the upstroke of each waveform, the foot can be found via the intersection of this line with the horizontal axis (time-to-foot method). The time difference between the feet of the two pressure waveforms provides the temporal distance, Δt. Given that the probes are separated by 10 cm, we can compute PWV by dividing the distance by Δt. While in PC MRI a single flow waveform is provided by any one acquisition, the high temporal resolution and numerous waveforms provided by the

Figure 2. Pressure waveforms provided by two fiber optic pressure sensors that sampled at a frequency of 1 kHz. The probes were separated by 10 cm and placed in the abdominal aorta of swine. The upstream probe was ~5 cm superior to the renal arteries, whereas the downstream probe was approximately 5 cm inferior to the renal arteries. Drift in the signal was due to respiration.

pressure probes can provide an individual PWV for every cycle recorded from the pressure probes. Thus, PWV can be recorded as the average value computed over numerous cardiac cycles. A MatLab-based software tool (MathWorks, Natick, MA) was developed to automatically identify the waveform peaks within every cardiac cycle in the pressure waveforms and to automatically compute and average the PWV from all cardiac cycles using the time-to-foot method.

MRI

Swine were imaged on a 3T clinical MR scanner (MR750, GE Healthcare, Waukesha, WI) using a 32-channel torso coil (NeoCoil, Pewaukee, WI). A contrast-enhanced angiogram was acquired in the abdominal vasculature; scan parameters were: $1\times$ dose (0.1 mmol/kg) gadobenate dimeglumine at an injection rate of 3 mL/s and a 20-mL flush, relaxation time / echo time (TR/TE) / flip angle = 3.52/1.16 msec/28°, field of view (FOV) = 44 × 44 cm², slice thickness = 1.8 mm with 0.9 mm spacing between slices, bandwidth = 325.5 Hz/pixel, 512 × 512 encoding matrix, breath-holding, in-plane spatial resolution = 0.86 × 0.86 mm². Reformatted images from the angiogram were used to place double oblique 2D PC slices.

2D PC data were acquired with a product sequence with prospective cardiac gating and rectilinear k-space sampling. Five evenly spaced slices were prescribed along the lower thoracic and abdominal aorta using reformatted images from the contrast-enhanced angiogram (slice placement is shown in Fig. 1b on the CT angiograms for reference). The series of 2D PC slices were acquired following a $1\times$ dose of gadobenate dimeglumine, as described above. Typical scan parameters were: VENC = 125 cm/s, through-plane velocity encoding, TR/TE/flip = 6.22 msec/3.45 msec/20°, FOV = 34 × 34 cm², slice thickness = 6 mm, bandwidth = 244 Hz/pixel, 256 × 256 encoding matrix, breath-holding, temporal resolution = ~12.4 msec, in-plane spatial resolution = 1.33 × 1.33 mm².

2D PC data were also acquired with a custom sequence with retrospective cardiac gating and radial k-space sampling. Five evenly spaced slices were placed using the identical slice prescriptions from the product 2D PC data above. Typical scan parameters were: VENC = 125 cm/s, through-plane velocity encoding, TR/TE/flip = 6.3 msec/3.5 msec/15°, FOV = 32 × 32 cm², slice thickness = 5 mm, bandwidth = 488 Hz/pixel, 256 × 256 encoding matrix, breath-holding, in-plane spatial resolution = 1.25 × 1.25 mm². During postprocessing, data were reconstructed into cardiac phases with a duration of 3*TR, which provided a temporal resolution = ~19 msec.

4D PC data were acquired with a dual-echo 5-point velocity-encoded sequence with radial undersampling in combination with retrospective electrocardiogram (ECG) gating (45–47). A $1\times$ dose of gadobenate dimeglumine was injected prior to the 4D PC acquisition with the same protocol described above; the use of contrast in the acquisition of 4D PC data provides improved signal-to-noise in magnitude images and noise reduction in velocity images (48). 4D PC data were acquired in the abdomen with the FOV centered on the takeoff of the renal arteries (Fig. 1b). Typical scan parameters were: VENC = 125 cm/s, three-directional velocity encoding, TR/TE/flip = 6.1 msec/2.4 msec/8°, reconstructed imaging volume = 34 × 34 × 34 cm³, bandwidth = 488.3 Hz/pixel, readout = 256 samples, resulting in 1.32 mm isotropic spatial resolution. The acquisition was conducted with an axial excitation and a slab thickness of 16 cm. Respiratory gating with a bellow signal was used with a 50% acceptance window that continuously adapted to the expiration position. The scan time was on the order of 10.5 minutes. During postprocessing, data were reconstructed into cardiac phases with a duration of 5*TR with temporal filtering in the RR-cycle (49), similar to view sharing, to yield a temporal resolution of ~31 msec on average. This filter provides a temporal window equal to ~31 msec in the central spatial frequencies of k-space and a temporal window equal to 5*31 = 155 msec in the higher frequency regions of k-space.

Histology

After the MR exam animals were euthanized with saturated potassium chloride administered intravenously. Subsequently, the aorta was localized, dissected, removed, and placed in formalin; the tissue samples were not pressure perfused. Tissue sections were stained with hematoxylin and eosin (H&E). For the injured group of swine, both injured and uninjured areas of the aortae were evaluated with histology (D.S.; 20 years of experience); histological slides were evaluated for lipid deposition, intimal-medial thickening, raised atheromatous lesions, infiltration of inflammatory cells, and the presence of fibrous and/or calcified regions.

Data Analysis

Pulse wave velocity was measured from the 4D PC and radial and Cartesian 2D PC sets of data, as

Figure 3. Scatter- and boxplots of pulse wave velocity (PWV) values measured from a 4D phase contrast (4D PC) technique, as well as gold standard fiber optic intravascular pressure probes, in swine with and without injury to the abdominal aorta. Both boxes and individual points are shown for each group. PWV values in the injured group were significantly greater than values in the uninjured group for both the 4D PC technique ($P = 0.03$) and the pressure probe measurements ($P = 0.02$). Press., Pressure.
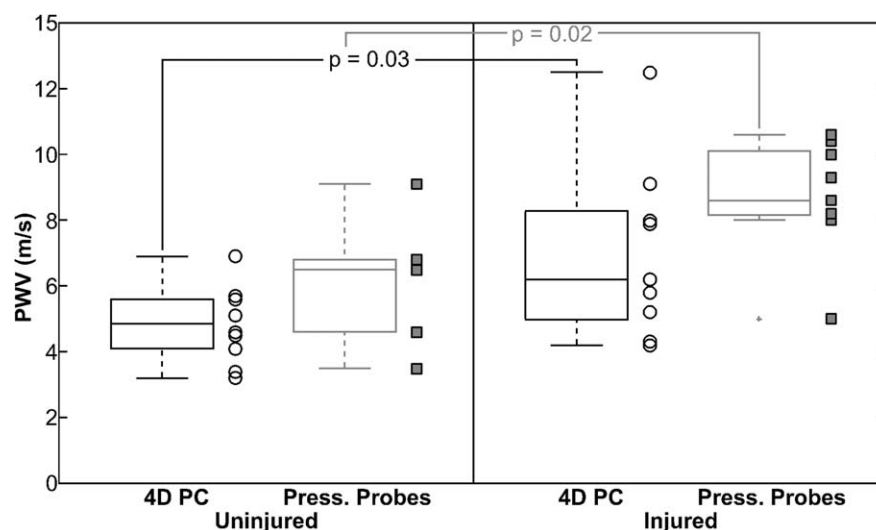
described previously (50). Briefly, PWV was computed first by identifying the temporal shift between flow waveforms at different locations; the distance between the slice locations from which these two flow waveforms were derived was divided by the temporal shift to yield the PWV. Reported PWV values were taken as the average PWV from the three techniques; one of the techniques was excluded from the average if the algorithm failed (eg, a poor time-to-foot fit due to an unusual shape of the flow waveform). Wall shear stress was measured in the abdominal aorta from the 4D PC data as described previously (51). Briefly, WSS was evaluated by computing the change in velocity at the vessel wall as a function of distance and multiplying it by blood viscosity. WSS values were averaged over three vertical segments (Fig. 1c)—upper, middle, and lower. The upper and lower segments represented the injured areas in the supra- and infrarenal aorta; the middle segment represented the uninjured area proximal to the ostia of the renal arteries.

Statistical Analysis

PWV measurements from the pressure probes, 4D PC, and radial and Cartesian 2D PC datasets were compared between the injured and uninjured animals with a nonpaired equal-variance Student's *t*-test ($P < 0.05$). PWV measurements from the 4D PC and radial and Cartesian 2D PC datasets were compared to the gold standard pressure probe-based PWV measurements with Bland–Altman analysis (52).

Average WSS measurements were evaluated within the uninjured and injured groups via paired Student's *t*-tests ($P < 0.05$) to compare the upper versus the middle segments, the middle versus the lower segments, and the upper versus the lower segments. Unpaired equal-variance Student's *t*-tests ($P < 0.05$) were also used to compare WSS measurements for each the upper, middle, and lower segments between the injured and uninjured groups.

RESULTS

C-Arm CT

C-arm CT provided images of the vasculature (Fig. 1) with 0.29 mm isotropic spatial resolution. For the injured animals, most angiograms were unremarkable. For the worst case, slight irregularities could be appreciated in the areas of injury, especially in the suprarenal abdominal aorta (Fig. 1d), but no frank stenoses were identified in the images.

MRI and Pressure Probes

Pressure probes measurements were obtained in 15/19 swine. The pressure probe system was not yet available for the first three uninjured swine; for one uninjured animal there were technical difficulties with the pressure probe system and pressure measurements could not be obtained. PWV measurements could not be obtained in two Cartesian 2D PC datasets (one uninjured and one injured swine) due to the absence of a systolic upstroke in each flow waveform, which may occur with the use of prospective cardiac gating. All measurements were successfully obtained with the radial 2D PC and 4D PC techniques, both of which utilized retrospective cardiac gating.

For PWV measurements obtained with the gold standard fiber optic intravascular pressure probes (Fig. 3), values in the uninjured swine (mean ± 1 SD = 6.2 ± 1.9 m/s) were significantly less than values in the injured swine (mean ± 1 SD = 8.7 ± 1.7; $P = 0.02$). Similarly, PWV measurements obtained with the 4D PC technique (Fig. 3) were significantly lower in the uninjured swine (mean ± 1 SD = 4.9 ± 1.1 m/s) than in the injured swine (mean ± 1 SD = 7.0 ± 2.7; $P = 0.03$). However, no significant differences were detected in comparing PWV values in uninjured and injured swine for both the radial 2D PC (mean ± 1 SD uninjured vs. injured = 7.4 ± 4.0 vs. 7.0 ± 2.6 m/s; $P = 0.83$) and Cartesian 2D PC (mean ± 1 SD uninjured vs. injured = 8.5 ± 4.1 vs. 7.9 ± 3.6 m/s; $P = 0.75$)
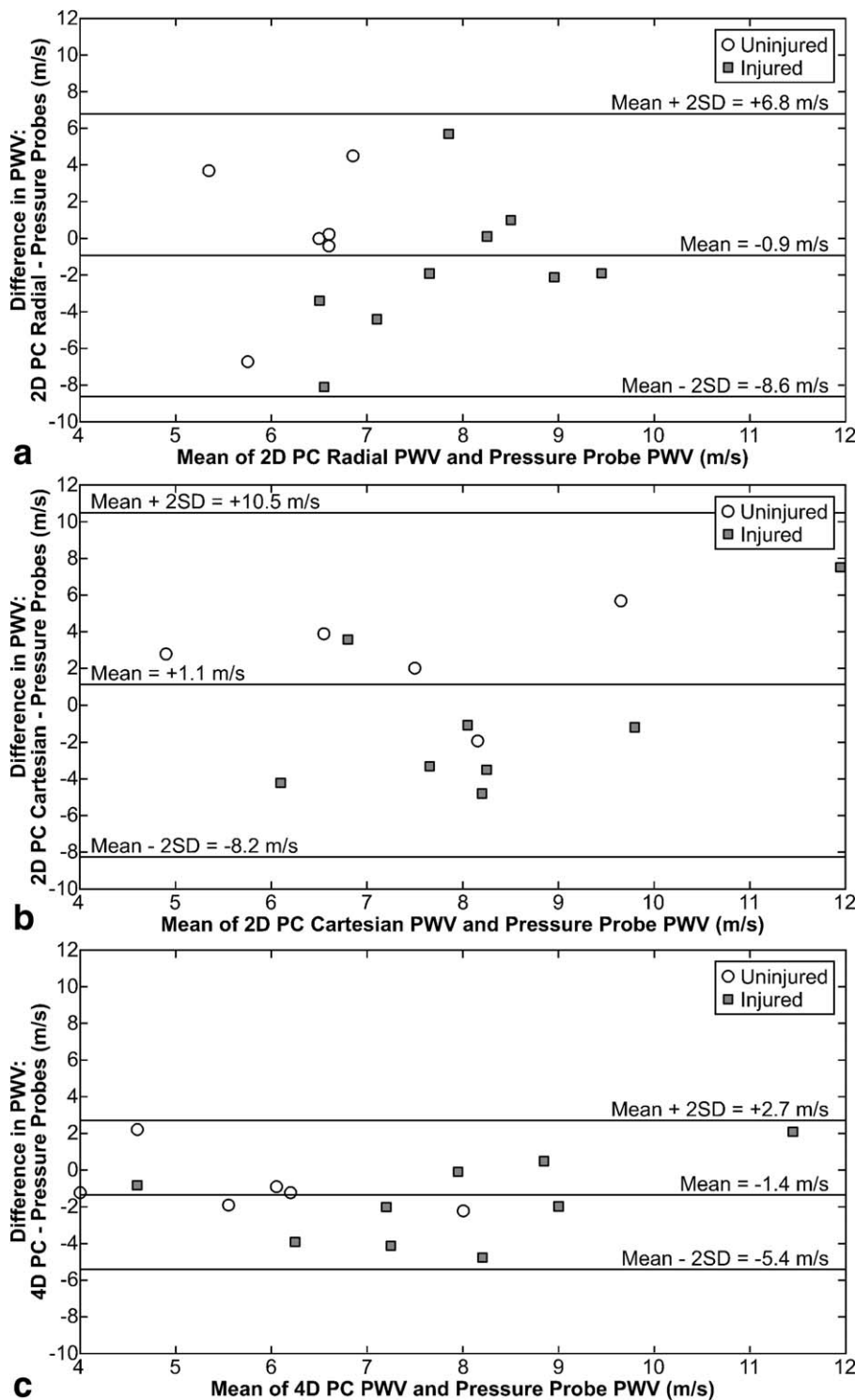
Figure 4. Bland–Altman analysis comparing pulse wave velocity (PWV) measurements derived from radial 2D PC (**a**), Cartesian 2D PC (**b**), and 4D PC (**c**) to gold standard pressure probe-based measurements of PWV. The mean bias (± 2 SD) was -0.9 ± 7.7, $+1.1 \pm 9.4$, and -1.4 ± 4.1 m/s for the radial 2D PC, Cartesian 2D PC, and 4D PC techniques, respectively.

techniques (data not shown). In Bland–Altman analysis, the radial 2D PC (Fig. 4a) and 4D PC (Fig. 4c) techniques tended to underestimate PWV values compared to measurements obtained from the pressure probes, with mean Bland–Altman biases (mean difference ± 2 SD) of -0.9 ± 7.7 and -1.4 ± 4.1 m/s, respectively. Conversely, Cartesian 2D PC (Fig. 4b) tended to overestimate PWV values compared to pressure probe measurements, with a mean Bland–Altman bias (mean difference ± 2 SD) of $+1.1 \pm 9.4$ m/s.

Mean (± 1 SD) WSS measurements (Fig. 5) in uninjured swine were 0.327 ± 0.084, 0.283 ± 0.081, and 0.223 ± 0.081 Pa for the upper, middle, and lower segments, respectively. Similarly, WSS measurements in injured swine were 0.338 ± 0.033, 0.306 ± 0.052, and 0.265 ± 0.042 Pa for the upper, middle, and lower segments, respectively. No significant differences were found between WSS measurements in uninjured and injured swine for the upper ($P = 0.73$), middle ($P = 0.47$), or lower ($P = 0.18$) segments. Within the group of

Figure 5. Boxplots of wall shear stress in uninjured and injured swine, in which the upper segment corresponds to the suprarenal abdominal aorta, the middle segment corresponds to the pararenal aorta, and the lower segment corresponds to the infrarenal abdominal aorta. In the injured group, the upper and lower segments align with areas of injury with a balloon catheter.
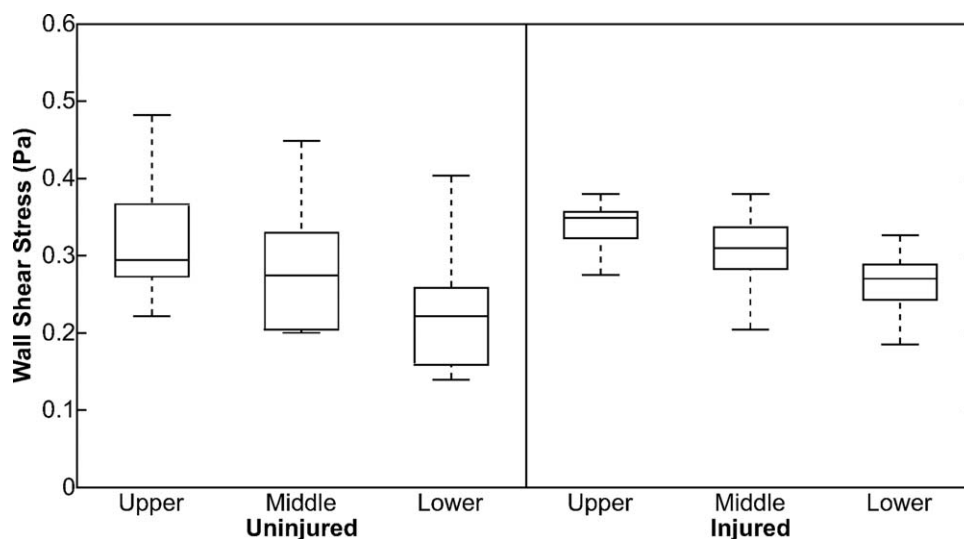
uninjured swine, the upper segment had significantly greater WSS values than the middle ($P = 2.8 \times 10^{-2}$) and lower ($P = 3.0 \times 10^4$) segments; additionally, WSS measurements in the middle segment were significantly larger than measurements in the lower segment ($P = 2.0 \times 10^{-4}$). Similarly in the group of injured swine, WSS values in the upper segment were significantly larger than values in the middle ($P = 0.04$) and lower ($P = 1.86 \times 10^{-6}$) segments; also, WSS measurements in the middle segment were significantly larger than measurements in the lower segment ($P = 9.8 \times 10^{-3}$).

Histology

Histological analysis of H&E-stained sections of uninjured aortae (Fig. 6a,b) revealed that the FH swine at
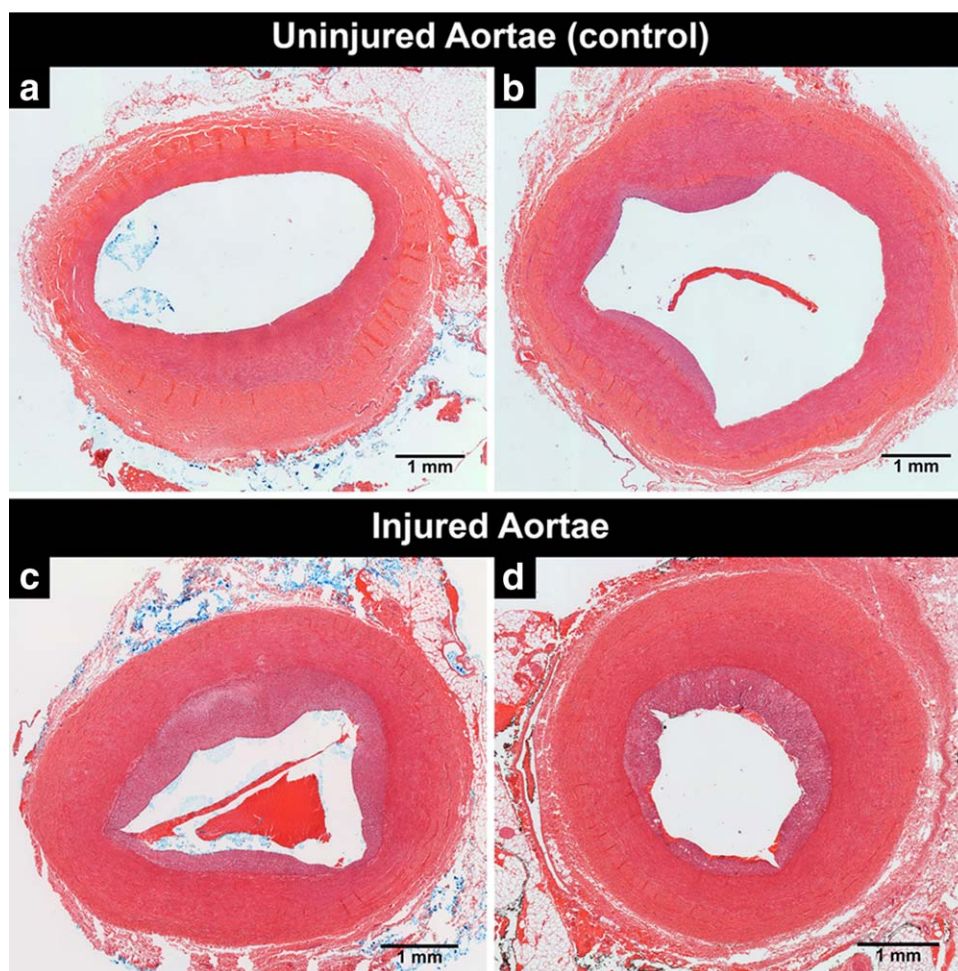
Figure 6. Hematoxylin and eosin (H&E) stain of slices extracted from the infrarenal abdominal aorta of uninjured (**a,b**) and injured (**c,d**) FH swine with a balloon catheter-induced injury. Each of the four slices shown was extracted from a different animal. Most swine with an injured aorta demonstrated substantial plaque development and intimal wall thickening (**c,d**). Uninjured swine demonstrated minimal (**b**) to no (**a**) plaque development in the same regions of the aorta.

8–11 months of age already have some, but minimal and variable degrees of, spontaneously developing atherosclerosis in the suprarenal and infrarenal regions of the abdominal aorta. In general, the disease process at this stage can be characterized by intimal (and some medial) thickening with a minimal number of plaques that protrude into the lumen. In contrast, the angioplasty balloon injury to the aortae resulted in a higher degree of lesion development in the same aortic regions (Fig. 6c,d). These injured regions in most of the animals examined histologically appear to have greater plaque volume in comparison to the same regions in the uninjured animals. The injury-induced plaques can be characterized as being in an early stage of development. In general, the injured regions show intimal thickening with the accumulation of foam cells and the presence of cholesterol clefts. Foci of inflammation were also seen in the atheromatous regions, with early signs of apoptotic regions. However, no noticeable signs of calcification were observed. It was also noted that a few of the injured animals did not develop as extensive disease as the others.

DISCUSSION

This study demonstrates our attempt at validating PWV measurements derived from 4D PC MRI, as well as radial and Cartesian 2D PC MRI, against gold standard pressure probe-based PWV measurements in a swine model of FH. Some validation of MRI-based PWV measurements have been performed (53,54), but not with a 4D PC technique. Additionally, this study was our initial attempt to create an aortic injury model, to elevate the PWV values in swine, and to analyze the effects of the injury on WSS.

In terms of noninvasive imaging, DSA is the standard means of detecting stenoses and evaluating vascular integrity. While 3D DSA images showed a minimal amount of vascular irregularity, there is a degree of bias in this evaluation, given that the location of vascular irregularity is known and expected due to the use of balloon catheter-induced injury. Given the limited extent to which vascular anomalies can be appreciated in these injured swine via 3D DSA, it would be encouraging to identify image-derived biomarkers that could differentiate a diseased from a nondiseased state before substantial changes occur with angiography. PWV is one such biomarker that holds this potential.

As hypothesized, the balloon catheter employed in the abdominal vasculature should create injury, leading to plaque development, increased stiffness, and thus, elevated PWV. It is encouraging that significant increases in PWV were detected in the injured group using both the pressure probes and 4D PC technique. However, significant differences between the uninjured and injured group were not detected with the radial and Cartesian 2D PC techniques.

The 4D PC MRI and the radial 2D PC MRI techniques underestimated PWV, and the Cartesian 2D PC MRI techniques overestimated PWV, compared to the gold standard pressure probe-based PWV measurements, as evidenced from Bland–Altman analysis. Inaccuracies in the MR-based measurements of PWV are likely secondary to both lower temporal resolution ($\sim$12.4–31 msec) and temporal blurring from the acquisition of MR data over numerous heartbeats; in comparison, the pressure probes provided a temporal resolution of 1 msec and thus acquired data in real time over numerous cardiac cycles. Nevertheless, the 95% limits of agreement for the 4D PC MRI Bland–Altman differences were substantially lower than the limits of agreement for the radial and Cartesian 2D PC PWV measurements. The discrepancy between 2D and 4D PC data is likely due to the difference in which data are analyzed. With 2D PC data the planes are selected at the time of acquisition. Thus, if five slices are acquired, only five different flow waveforms can be measured. With the low temporal resolution compared to the pressure probes, the sampling of one or more of those flow waveforms can on occasion cause the waveform to appear shifted relative to the waveforms from other slices. Thus, computing PWV is highly dependent on how the waveforms are sampled from one plane to another. Furthermore, the shapes of waveforms vary substantially as the aorta is traversed, especially in the abdomen. Thus, the shape can cause substantial changes to the time-to-foot fit, as well as the time-to-upstroke and cross-correlation methods of computing PWV. Since the 2D slices are determined at the time of acquisition, planes with flow waveforms of a consistent shape cannot be selected a posteriori. In comparison, the planes from 4D PC MRI are all from a single dataset and thus it is less likely that sampling of the flow waveforms will vary from one plane to the next. Therefore, PWV computation is likely to be more consistent. Additionally, the selection of planes is performed after the acquisition; this allows for planes to be selected that provide as consistent a shape as possible for the flow waveforms. While 4D PC MRI provides lower temporal resolution than the 2D PC techniques, the ability to select planes during the analysis and the consistency of sampling allowed for better overall PWV measurements with less variability.

Differences in PWV between the injured and uninjured swine are statistically significant with the 4D PC and pressure probe data. However, significant differences were not found between groups using either the radial or Cartesian 2D PC MRI techniques. As described above, variations from slice to slice made the series of 2D PC slices more prone to outlying PWV measurements. Such variability mitigated potential differences between the uninjured and injured swine as measured with the 2D PC techniques.

WSS measurements decreased progressively from the upper, middle, and lower segments as expected, given that blood velocity decreases as the aorta is traversed and that WSS is dependent on blood velocity. No significant differences were found in comparing WSS measurements between the uninjured and injured groups. Within both the uninjured and injured groups, each segment was significantly different than the other. While not revealed statistically, it

is interesting to note that the differences between segments in the injured group was suppressed compared to the uninjured group. The creation of injury in the upper and lower segments in the injured group may have led to this suppression, yet it is difficult to determine the factors that lead to our measured WSS values. In terms of atherosclerosis, WSS is largely a predictive biomarker, such that areas of low flow lead to low WSS, which in turn leads to endothelial dysfunction (12). As the plaques develop secondary to endothelial dysfunction, the vessel radius will eventually decrease, which serves to elevate the WSS via an increase in blood velocity. In this study plaques were predominantly created via injury. Since plaques were created artificially the plaques are not due to low flow and therefore the areas of plaque should not have low WSS values. As plaques develop the WSS should increase due to increases in velocity secondary to narrowing of the vessel lumen; but at 4 weeks postinjury there is likely to be outward remodeling of the vessels (Glagov phenomenon) (55), and therefore no substantial changes to the vessel radius. Nevertheless, the suppression of WSS between segments in the injured swine is an interesting result that warrants further investigation.

One limitation of this study is that the presence of spontaneously developing atherosclerosis in some of the uninjured animals may have mitigated differences in PWV and WSS between the injured and uninjured groups. Additionally, the lower degree of lesion development in a few of the injured animals may also have mitigated differences between groups. We believe that the chosen sizes of balloon used to cause the injury in some of these animals may have been too small for the aortic lumen; that is, the extent of injury induced may have been smaller than in the other animals. In future studies these limitations can be overcome by 1) using younger FH swine (∼4 months of age) that typically do have noticeable development of atherosclerosis in the aortae via histology, and 2) selecting sizes of balloons that are specifically suited to the size of the aorta in each animal (determined fluoroscopically prior to injury induction). Furthermore, it is unknown how naturally developed plaques in these hypercholesterolemic swine differ from artificially created plaques and what effect these differences would have on PWV and WSS measurements. While the animals are homozygous for FH and do indeed develop plaques naturally over time, the animals are too large for the MRI scanner bore by the time plaques have developed sufficiently and substantially. Even though the animals are relatively small via cross-breeding with miniaturized swine, the animals were too large circumferentially for the scanner by 12–18 months of age for this study. In future studies, this limitation may be overcome by limiting the size of the animals via careful management of energy balance or by imaging the animals by the time they reach sexual maturity or near the maximum size accommodated by the scanner. The injury protocol helps to ensure reproducibility of the plaque in both size and location. In evaluating PWV from 4D PC data, 4–5 planes were selected in the vicinity of the planes prescribed for the

series of 2D PC images. However, these planes were not precisely registered between the 2D and 4D PC datasets. For data acquired with the Cartesian 2D PC MRI technique, PWV could not be derived from two subjects because a large portion of the systolic upstroke was absent from the flow waveforms in these two datasets. The use of prospective cardiac gating in standard Cartesian 2D PC acquisitions omits portions of the flow waveforms via the use of a trigger delay and arrhythmia rejection window (50). The use of retrospective cardiac gating, as employed in the radial 2D PC and 4D PC techniques, avoids this problem. A potential source of error when comparing PWV values between MR methods is the potential for variations in heart rate to confound PWV values, given that the heart rate will be different during each of the MR acquisitions (56). While this is a potential source of error in some anatomical locations, such as the thoracic aorta and lower extremities, other studies (57) have demonstrated that no significant relationship exists between heart rate and PWV in the abdominal aorta—the focus of this study. There were a total of 12 t-tests performed in this study; Bonferroni correction was not employed, as the authors considered this to be overly conservative given the small samples sizes in this study.

In conclusion, the 4D PC MRI technique provided the ability to derive both PWV and WSS from a single acquisition. The 4D PC MRI acquisition provided a promising means of computing PWV in a swine model of atherosclerosis, as evidenced by the lower variability of the data compared to 2D techniques and the similarity of the results compared to the gold standard pressure probes. The evaluation of WSS was successful, but the results were difficult to interpret based on the artificially created plaques used in this study design. The injury model for creating plaques was successful, with significantly elevated PWV values detected by both the 4D PC MRI technique and the gold standard pressure probes. Overall, 4D PC MRI is a promising acquisition for the evaluation of atherosclerosis; this study may provide a platform for developing the 4D PC MRI technique further for the early detection of atherosclerosis.

REFERENCES

1. Gaziano JM, Wilson PW. Cardiovascular risk assessment in the 21st century. JAMA 2012;308:816–817.
2. Den Ruijter HM, Peters SA, Anderson TJ, et al. Common carotid intima-media thickness measurements in cardiovascular risk prediction: a meta-analysis. JAMA 2012;308:796–803.
3. Yeboah J, McClelland RL, Polonsky TS, et al. Comparison of novel risk markers for improvement in cardiovascular risk assessment in intermediate-risk individuals. JAMA 2012;308:788–795.
4. Schmermund A, Erbel R. Unstable coronary plaque and its relation to coronary calcium. Circulation 2001;104:1682–1687.
5. Taylor AJ, Burke AP, O'Malley PG, et al. A comparison of the Framingham risk index, coronary artery calcification, and culprit plaque morphology in sudden cardiac death. Circulation 2000; 101:1243–1248.
6. Rodondi N, Auer R, Devine PJ, O'Malley PG, Hayoz D, Cornuz J. The impact of carotid plaque screening on motivation for smoking cessation. Nicotine Tob Res 2008;10:541–546.
7. Wong ND, Detrano RC, Diamond G, et al. Does coronary artery screening by electron beam computed tomography motivate

potentially beneficial lifestyle behaviors? Am J Cardiol 1996;78: 1220–1223.

8. Friedman MH, Deters OJ, Bargeron CB, Hutchins GM, Mark FF. Shear-dependent thickening of the human arterial intima. Atherosclerosis 1986;60:161–171.

9. Ku DN, Giddens DP, Phillips DJ, Strandness DE Jr. Hemodynamics of the normal human carotid bifurcation: in vitro and in vivo studies. Ultrasound Med Biol 1985;11:13–26.

10. Pedersen EM, Oyre S, Agerbaek M, et al. Distribution of early atherosclerotic lesions in the human abdominal aorta correlates with wall shear stresses measured in vivo. Eur J Vasc Endovasc Surg 1999;18:328–333.

11. Zarins CK, Giddens DP, Bharadvaj BK, Sottiurai VS, Mabon RF, Glagov S. Carotid bifurcation atherosclerosis. Quantitative correlation of plaque localization with flow velocity profiles and wall shear stress. Circ Res 1983;53:502–514.

12. Cheng C, Tempel D, van Haperen R, et al. Atherosclerotic lesion size and vulnerability are determined by patterns of fluid shear stress. Circulation 2006;113:2744–2753.

13. Laurent S, Katsahian S, Fassot C, et al. Aortic stiffness is an independent predictor of fatal stroke in essential hypertension. Stroke 2003;34:1203–1206.

14. Bock M, Schad LR, Muller E, Lorenz WJ. Pulsewave velocity measurement using a new real-time MR-method. Magn Reson Imaging 1995;13:21–29.

15. Harloff A, Nussbaumer A, Bauer S, et al. In vivo assessment of wall shear stress in the atherosclerotic aorta using flow-sensitive 4D MRI. Magn Reson Med 2010;63:1529–1536.

16. Frydrychowicz A, Stalder AF, Russe MF, et al. Three-dimensional analysis of segmental wall shear stress in the aorta by flow-sensitive four-dimensional-MRI. J Magn Reson Imaging 2009;30: 77–84.

17. Oshinski JN, Ku DN, Mukundan S Jr, Loth F, Pettigrew RI. Determination of wall shear stress in the aorta with the use of MR phase velocity mapping. J Magn Reson Imaging 1995;5:640–647.

18. Oyre S, Pedersen EM, Ringgaard S, Boesiger P, Paaske WP. In vivo wall shear stress measured by magnetic resonance velocity mapping in the normal human abdominal aorta. Eur J Vasc Endovasc Surg 1997;13:263–271.

19. Bogren HG, Buonocore MH. 4D magnetic resonance velocity mapping of blood flow patterns in the aorta in young vs. elderly normal subjects. J Magn Reson Imaging 1999;10:861–869.

20. Bogren HG, Mohiaddin RH, Kilner PJ, Jimenez-Borreguero LJ, Yang GZ, Firmin DN. Blood flow patterns in the thoracic aorta studied with three-directional MR velocity mapping: the effects of age and coronary artery disease. J Magn Reson Imaging 1997;7: 784–793.

21. Frydrychowicz A, Harloff A, Jung B, et al. Time-resolved, 3-dimensional magnetic resonance flow analysis at 3 T: visualization of normal and pathological aortic vascular hemodynamics. J Comput Assist Tomogr 2007;31:9–15.

22. Markl M, Draney MT, Hope MD, et al. Time-resolved 3-dimensional velocity mapping in the thoracic aorta: visualization of 3-directional blood flow patterns in healthy volunteers and patients. J Comput Assist Tomogr 2004;28:459–468.

23. Markl M, Draney MT, Miller DC, et al. Time-resolved three-dimensional magnetic resonance velocity mapping of aortic flow in healthy volunteers and patients after valve-sparing aortic root replacement. J Thorac Cardiovasc Surg 2005;130:456–463.

24. Markl M, Wallis W, Brendecke S, Simon J, Frydrychowicz A, Harloff A. Estimation of global aortic pulse wave velocity by flow-sensitive 4D MRI. Magn Reson Med 2010;63:1575–1582.

25. Goldberg AC, Hopkins PN, Toth PP, et al. Familial hypercholesterolemia: screening, diagnosis and management of pediatric and adult patients: clinical guidance from the National Lipid Association Expert Panel on Familial Hypercholesterolemia. J Clin Lipidol 2011;5:133–140.

26. Hasler-Rapacz J, Ellegren H, Fridolfsson AK, et al. Identification of a mutation in the low density lipoprotein receptor gene associated with recessive familial hypercholesterolemia in swine. Am J Med Genet 1998;76:379–386.

27. Rapacz J, Grummer RH, Hasler J, Shakelford RM. Allotype polymorphism of low density beta-lipoproteins in pig serum (LDLpp I, LDLpp 2). Nature 1970;225:941–942.

28. Rapacz J, Hasler-Rapacz J, Kuo WH, Li D. Immunogenetic polymorphism of lipoproteins in swine. 1. Four additional serum beta-lipoprotein allotypes (Lpp2, Lpp4, Lpp5 and Lpp15) in the Lpp system. Anim Blood Groups Biochem Genet 1976;7:157–177.

29. Thim T, Hagensen MK, Drouet L, et al. Familial hypercholesterolaemic downsized pig with human-like coronary atherosclerosis: a model for preclinical studies. EuroIntervention 2010;6:261–268.

30. Granada JF, Kaluza GL, Wilensky RL, Biedermann BC, Schwartz RS, Falk E. Porcine models of coronary atherosclerosis and vulnerable plaque for imaging and interventional research. EuroIntervention 2009;5:140–148.

31. Wernersson R, Schierup MH, Jorgensen FG, et al. Pigs in sequence space: a 0.66X coverage pig genome survey based on shotgun sequencing. BMC Genom 2005;6:70.

32. Humphray SJ, Scott CE, Clark R, et al. A high utility integrated map of the pig genome. Genome Biol 2007;8:R139.

33. Tellez A, Krueger CG, Seifert P, et al. Coronary bare metal stent implantation in homozygous LDL receptor deficient swine induces a neointimal formation pattern similar to humans. Atherosclerosis 2010;213:518–524.

34. Bahls M, Bidwell CA, Hu J, et al. Gene expression differences in healthy brachial and femoral arteries of Rapacz familial hypercholesterolemic swine. Physiol Genom 2011;43:781–788.

35. Bahls M, Bidwell CA, Hu J, et al. Gene expression differences during the heterogeneous progression of peripheral atherosclerosis in familial hypercholesterolemic swine. BMC Genom 2013;14: 443.

36. Ge W, Krueger CG, Weichmann A, Shanmuganayagam D, Varghese T. Displacement and strain estimation for evaluation of arterial wall stiffness using a familial hypercholesterolemia swine model of atherosclerosis. Med Phys 2012;39:4483–4492.

37. Schinkel AF, Krueger CG, Tellez A, et al. Contrast-enhanced ultrasound for imaging vasa vasorum: comparison with histopathology in a swine model of atherosclerosis. Eur J Echocardiol 2010;11:659–664.

38. Staub D, Schinkel AF, Coll B, et al. Contrast-enhanced ultrasound imaging of the vasa vasorum: from early atherosclerosis to the identification of unstable plaques. JACC Cardiovasc Imaging 2010;3:761–771.

39. Louis CF, Gallant EM, Remple E, Mickelson JR. Malignant hyperthermia and porcine stress syndrome: a tale of two species. Pig News Inform 1990;11:341–344.

40. Lerman J, Oyston JP, Gallagher TM, Miyasaka K, Volgyesi GA, Burrows FA. The minimum alveolar concentration (MAC) and hemodynamic effects of halothane, isoflurane, and sevoflurane in newborn swine. Anesthesiology 1990;73:717–721.

41. Wentland AL, Artz NS, Fain SB, Grist TM, Djamali A, Sadowski EA. MR measures of renal perfusion, oxygen bioavailability and total renal blood flow in a porcine model: noninvasive regional assessment of renal function. Nephrol Dial Transplant 2012;27: 128–135.

42. Ahmed AS, Zellerhoff M, Strother CM, et al. C-arm CT measurement of cerebral blood volume: an experimental study in canines. AJNR Am J Neuroradiol 2009;30:917–922.

43. Bley T, Strother CM, Pulfer K, et al. C-arm CT measurement of cerebral blood volume in ischemic stroke: an experimental study in canines. AJNR Am J Neuroradiol 2010;31:536–540.

44. Kao TW, Taylor HF. High-sensitivity intrinsic fiber-optic Fabry-Perot pressure sensor. Opt Lett 1996;21:615–617.

45. Gu T, Korosec FR, Block WF, et al. PC VIPR: a high-speed 3D phase-contrast method for flow quantification and high-resolution angiography. AJNR Am J Neuroradiol 2005;26:743–749.

46. Johnson KM, Lum DP, Turski PA, Block WF, Mistretta CA, Wieben O. Improved 3D phase contrast MRI with off-resonance corrected dual echo VIPR. Magn Reson Med 2008;60:1329–1336.

47. Johnson KM, Markl M. Improved SNR in phase contrast velocimetry with five-point balanced flow encoding. Magn Reson Med 2010;63:349–355.

48. Bock J, Frydrychowicz A, Stalder AF, et al. 4D phase contrast MRI at 3 T: effect of standard and blood-pool contrast agents on SNR, PC-MRA, and blood flow visualization. Magn Reson Med 2010;63:330–338.

49. Liu J, Redmond MJ, Brodsky EK, et al. Generation and visualization of four-dimensional MR angiography data using an under-sampled 3-D projection trajectory. IEEE Trans Med Imaging 2006;25:148–157.

50. Wentland AL, Wieben O, Francois CJ, et al. Aortic pulse wave velocity measurements with undersampled 4D flow-sensitive MRI: comparison with 2D and algorithm determination. J Magn Reson Imaging 2013;37:853–859.

51. Bieging ET, Frydrychowicz A, Wentland A, et al. In vivo three-dimensional MR wall shear stress estimation in ascending aortic dilatation. J Magn Reson Imaging 2011;33:589–597.

52. Bland JM, Altman DG. Statistical methods for assessing agreement between two methods of clinical measurement. Lancet 1986;1:307–310.

53. Grotenhuis HB, Westenberg JM, Steendijk P, et al. Validation and reproducibility of aortic pulse wave velocity as assessed with velocity-encoded MRI. J Magn Reson Imaging 2009;30:521–526.

54. Taviani V, Hickson SS, Hardy CJ, et al. Age-related changes of regional pulse wave velocity in the descending aorta using Fourier velocity encoded M-mode. Magn Reson Med 2011;65:261–268.

55. Glagov S, Weisenberg E, Zarins CK, Stankunavicius R, Kolettis GJ. Compensatory enlargement of human atherosclerotic coronary arteries. N Engl J Med 1987;316:1371–1375.

56. Lantelme P, Mestre C, Lievre M, Gressard A, Milon H. Heart rate: an important confounder of pulse wave velocity assessment. Hypertension 2002;39:1083–1087.

57. Sa Cunha R, Pannier B, Benetos A, et al. Association between high heart rate and high arterial rigidity in normotensive and hypertensive subjects. J Hypertens 1997;15(12 Pt 1):1423–1430.